Journal of The Electrochemical Society, **160** (1) E5-E11 (2013)
0013-4651/2013/160(1)/E5/7/$28.00 © The Electrochemical Society

Validation of Theory with Experiments for Local Mass Transfer at Parallel Plate Electrodes under Laminar Flow Conditions

A. N. Colli and J. M. Bisang[z]

Programa de Electroquímica Aplicada e Ingeniería Electroquímica (PRELINE), Facultad de Ingeniería Química, Universidad Nacional del Litoral, Santiago del Estero 2829, S3000AOM Santa Fe, Argentina

Theoretical equations are reported to calculate the local Sherwood number for a parallel plate electrochemical reactor with a developing flow region under laminar flow conditions. These equations were deduced from analytical velocity profiles according to different proposals, which are compared with the velocity profiles given by the numerical solution of the Navier-Stokes equations. A comparison between the theoretical mass transfer equations with experimental results is also given.
 [DOI: 10.1149/2.015302jes]

Manuscript submitted October 11, 2012; revised manuscript received November 12, 2012. Published November 14, 2012.

Parallel plate electrodes assembled in a filter press configuration are frequently used in the industrial practice either in monopolar or bipolar connection. These reactors present as advantages: (i) simplified constructive features, (ii) the interelectrode gap is uniform and can be defined by a single and easily adjustable geometric variable, and (iii) the primary and secondary current distributions are uniform. However, the mass transfer characteristics change along the electrode length and considerable edge effects can occur near the inlet and outlet of the electrolyte to the reactor, which requires the examination of the local mass transfer coefficient to characterize the reactor performance. Likewise, the interelectrode gap must be small to diminish the ohmic drop in the solution phase, which becomes more important for the processing of low conductivity electrolytes as in the reactors for organic electrosynthesis or for drinking water disinfection. The modeling of parallel plate electrochemical reactors was outlined in previous papers.[1,2] Likewise, for infinitely wide electrodes, the local mass transfer coefficient with fully developed flow was reported by Pickett[3] and by Moldoveanu[4] for different conditions imposed at the wall surfaces. The case of thin-gap channel flow cells was analyzed by Edwards and Newman.[5] Georgiadou[6,7] developed a numerical method for a parallel plate electrochemical reactor involving the terms of ionic migration. Electrodes of finite width with fully developed flow were also modeled.[3,8–10] The study of mass transfer in developing flow, in which the electrodes are located just downstream of the electrolyte inlet, requires the simultaneous solution of the mass and momentum transfers. This configuration is typical of industrial reactors, where no entrance length is used and the mass transfer conditions are enhanced. Thus, the influence of hydrodynamic and entrance effects on the performance of a parallel plate electrochemical reactor was studied,[11,12] where the mass transfer under developing laminar flow was represented by empirical equations. Recently, Vázquez[13] treated the problem of the developing flow in electrochemical reactors by computational fluid dynamics using a commercial code to calculate the velocity and also mass transport profiles[14] for the FM01-LC parallel plate cell, a scaled down version of the FM21-SP reactor used in the chlor-alkali industry.

The aim of the present contribution is to develop analytical equations for the variation of the local mass transfer coefficient along the axial coordinate in parallel plate electrochemical reactors under laminar flow conditions. The hydrodynamic entrance effect is considered taking into account theoretical velocity profiles. A comparison is performed between these theoretical equations with that from the numerical solution of the hydrodynamic equations and also with experimental measurements to determine their predictive capabilities.

Mathematical Model

A schematic view of the model is shown in Figure 1. The temporal behavior of an electrochemical reactor with infinitely wide parallel plate electrodes in presence of supporting electrolyte is given by the convective mass transfer equation as

$$\frac{\partial C}{\partial T} + V_x \frac{\partial C}{\partial X} + V_y \frac{\partial C}{\partial Y} = \frac{1}{\mathrm{ReSc}} \left(\frac{\partial^2 C}{\partial X^2} + \frac{\partial^2 C}{\partial Y^2} \right) \quad [1]$$

Assuming that

$$\frac{\partial^2 C}{\partial Y^2} \gg \frac{\partial^2 C}{\partial X^2} \quad [2]$$

and for steady-state conditions, equation 1 is simplified to

$$V_x \frac{\partial C}{\partial X} + V_y \frac{\partial C}{\partial Y} = \frac{1}{\mathrm{ReSc}} \frac{\partial^2 C}{\partial Y^2} \quad [3]$$

with the following boundary conditions

$$X = 0 \quad C(0, Y) = 1 \quad [4]$$

$$Y = 0 \quad C(X, 0) = C_s \quad [5]$$

At the central part of the reactor

$$C(X, Y) = 1 \quad [6]$$

The dimensionless velocity can be represented by a Taylor series expansion ignoring terms of second and higher order as

$$V_x(X, Y) = V_x(X, 0) + Y \left. \frac{\partial V_x}{\partial Y} \right|_{Y=0} = Y\varepsilon \quad [7]$$

being

$$\varepsilon = \left. \frac{\partial V_x}{\partial Y} \right|_{Y=0} \quad [8]$$

Equations 6 and 7 are valid because the thickness of the diffusion boundary layer is smaller than that of the hydrodynamic boundary layer, due to the high value of the Schmidt number for electrochemical systems.

For incompressible fluids, the continuity equation is

$$\frac{\partial V_x}{\partial X} + \frac{\partial V_y}{\partial Y} = 0 \quad [9]$$

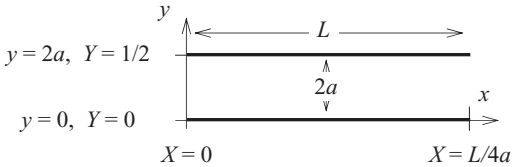

Figure 1. Schematic view of the parallel plate electrochemical reactor and coordinates.

[z]E-mail: jbisang@fiq.unl.edu.ar.

Combining equations 7 and 9 and solving results in

$$V_y(X, Y) = -\frac{Y^2}{2}\frac{d\varepsilon}{dX} \quad [10]$$

Introducing equations 7 and 10 into equation 3 yields

$$Y\varepsilon\frac{\partial C}{\partial X^*} - \frac{Y^2}{2}\frac{d\varepsilon}{dX^*}\frac{\partial C}{\partial Y} = \frac{1}{Sc}\frac{\partial^2 C}{\partial Y^2} \quad [11]$$

being

$$X^* = \frac{X}{Re} \quad [12]$$

Defining a combined variable, ξ, as[15]

$$\xi = Y\sqrt{\varepsilon}\left[\frac{Sc}{9\int_0^{X^*}\sqrt{\varepsilon}dX^*}\right]^{1/3} \quad [13]$$

Equation 11 is transformed to the ordinary differential equation

$$\frac{d^2C}{d\xi^2} = -3\xi^2\frac{dC}{d\xi} \quad [14]$$

with the boundary conditions

$$\xi = 0 \quad C(0) = C_s \quad [15]$$

$$\xi \to \infty \quad C(\infty) = 1 \quad [16]$$

Solving equation 14 yields

$$\frac{dC}{d\xi} = \frac{1 - C_s}{\Gamma(4/3)}\exp(-\xi^3) \quad [17]$$

The local Sherwood number is defined as

$$Sh_x = \frac{k_{m,x}d_h}{D} \quad [18]$$

where the local mass transfer coefficient is given by

$$k_{m,x} = \frac{D}{d_h(1 - C_s)}\left.\frac{\partial C}{\partial Y}\right|_{Y=0} = \frac{D}{d_h(1 - C_s)}\left.\frac{dC}{d\xi}\right|_{\xi=0}\left.\frac{\partial \xi}{\partial Y}\right|_{Y=0} \quad [19]$$

Introducing equation 19 into equation 18 yields

$$Sh_x = \frac{1}{(1 - C_s)}\left.\frac{dC}{d\xi}\right|_{\xi=0}\left.\frac{\partial \xi}{\partial Y}\right|_{Y=0} \quad [20]$$

Combining equation 17, evaluated at $\xi = 0$, with the first derivative of equation 13 and equation 20 results in

$$Sh_x = \frac{\sqrt{\varepsilon}}{\Gamma(4/3)}\left(\frac{Sc}{9\int_0^{X^*}\sqrt{\varepsilon}dX^*}\right)^{1/3} \quad [21]$$

The hydrodynamic regime inside the reactor is given by the Navier-Stokes equations:

$$\frac{\partial V_x}{\partial T} + V_x\frac{\partial V_x}{\partial X} + V_y\frac{\partial V_x}{\partial Y} = -\frac{\partial P}{\partial X} + \frac{1}{Re}\left[\frac{\partial^2 V_x}{\partial X^2} + \frac{\partial^2 V_x}{\partial Y^2}\right] \quad [22]$$

$$\frac{\partial V_y}{\partial T} + V_x\frac{\partial V_y}{\partial X} + V_y\frac{\partial V_y}{\partial Y} = -\frac{\partial P}{\partial Y} + \frac{1}{Re}\left[\frac{\partial^2 V_y}{\partial X^2} + \frac{\partial^2 V_y}{\partial Y^2}\right] \quad [23]$$

Thus, to calculate the local Sherwood number it is necessary to introduce into equation 21 the function ε, which requires the simultaneous solution of equations 9, 22 and 23.

Theoretical Models Based on Analytical Velocity Profiles

Parallel plate reactor with fully developed laminar flow.— In this case the solution of equation 22,[16] is

$$V_x = 12Y(1 - 2Y) \quad [24]$$

Combining equations 8 and 24 is

$$\varepsilon = 12 \quad [25]$$

Introducing equation 25 into equation 21 and rearranging results in

$$Sh_x = 1.232\left(\frac{Sc}{X^*}\right)^{1/3} \quad [26]$$

and the average Sherwood number, Sh, is given by

$$Sh = \frac{d_h}{L}\int_0^{L/d_h} Sh_x dX = 1.85\left(ReSc\frac{d_h}{L}\right)^{1/3} \quad [27]$$

Equations 26 and 27 were previously reported by Pickett.[3]

Developing laminar flow according to the boundary layer theory[17].— The velocity profile is given by

$$V_x = \frac{3d_h}{2\delta_h}Y - \frac{1}{2}\left(\frac{d_h}{\delta_h}Y\right)^3 \quad [28]$$

being

$$\delta_h = 4.64d_h\left(X^*\right)^{1/2} \quad [29]$$

Combining equations 8, 28 and 29 is

$$\varepsilon = \frac{0.323}{\left(X^*\right)^{1/2}} \quad [30]$$

Introducing equation 30 into equation 21 and solving results in

$$Sh_x = 0.335\frac{Sc^{1/3}}{\left(X^*\right)^{1/2}} \quad [31]$$

The average Sherwood number is now given by

$$Sh = 0.664\left(Re\frac{d_h}{L}\right)^{1/2}Sc^{1/3} \quad [32]$$

Equivalent expressions to equations 31 or 32 were also deduced by Eckert and Drake[18] and Levich.[19]

Developing laminar flow according to the procedure of Han[20] *and Glasgow*[21].— Linearizing equation 22 and taking into account equation 9, Han[20] has proposed the velocity profile for a parallel plate system with aspect ratio zero, which in terms of the hydraulic diameter and Y is given by

$$V_x = \frac{\cosh(\beta d_h/4) - \cosh[\beta d_h(Y - 1/4)]}{\cosh(\beta d_h/4) - 4\sinh(\beta d_h/4)/(\beta d_h)} \quad [33]$$

Introducing the first derivative of equation 33, evaluated at $Y = 0$, into equation 8 yields

$$\varepsilon = \frac{\beta^2 d_h}{\beta\coth(\beta d_h/4) - 4/d_h} \quad [34]$$

The function β can be obtained by integration of the following equation according to the procedure outlined by Glasgow[21]

$$\int_\infty^\beta \frac{d\phi}{d\beta}\frac{1}{\gamma}d\beta = X^* \quad [35]$$

being

$$\gamma = (\beta d_h)^2\left[\frac{\operatorname{sech}(\beta d_h/4)/4 - \tanh(\beta d_h/4)/(\beta d_h)}{1 - \tanh(\beta d_h/4)/(\beta d_h/4)}\right] \quad [36]$$

and

$$\phi = \frac{1/8 + \operatorname{sech}(\beta d_h/4)/4 - 3/2\tanh(\beta d_h/4)/(\beta d_h)}{\left[1 - \tanh(\beta d_h/4)/(\beta d_h/4)\right]^2} \quad [37]$$

Introducing equation 34 into equation 21 yields

$$Sh_x\, Sc^{-1/3} = \frac{\beta d_h^{1/2}\left[\beta\coth(\beta d_h/4) - 4/d_h\right]^{-1/2}}{\Gamma(4/3)\left\{9\int_0^{X^*}\beta d_h^{1/2}/\left[\beta\coth(\beta d_h/4) - 4/d_h\right]^{1/2} dX^*\right\}^{1/3}} \quad [38]$$

Developing laminar flow according to the Sparrow[22] model for the velocity profile.— This model assumes that the velocity boundary layer grows in thickness along the length of the electrode until it reaches the center line, where it meets the boundary layer from the other electrode. Thus, the velocity inside the diffusion layer can be approximated by

$$V_x = V_{max}\left[2\frac{d_h Y}{\delta_h} - \left(\frac{d_h Y}{\delta_h}\right)^2\right] \quad [39]$$

being

$$\delta_h = \frac{3}{4}d_h\left(1 - \frac{1}{V_{max}}\right) \quad [40]$$

Then

$$\varepsilon = \frac{8V_{max}^2}{3(V_{max} - 1)} \quad [41]$$

V_{max} must be obtained for each X^* value from the integral equation

$$X^* = \frac{3}{160}\int_0^{V_{max}} \frac{(V_{max} - 1)(9V_{max} - 7)}{V_{max}^2} dV_{max} \quad [42]$$

At high X^* values, $\delta_h \to a$ and $\varepsilon \to 12$, which agrees with the fully developed laminar flow model.

Introducing equation 41 into equation 21 yields

$$Sh_x\, Sc^{-1/3} = \frac{2V_{max}/(V_{max} - 1)^{1/2}}{3\Gamma(4/3)\left[\int_0^{X^*} V_{max}/(V_{max} - 1)^{1/2} dX^*\right]^{1/3}} \quad [43]$$

Developing laminar flow according to the Sparrow and coworkers[23] model for the velocity profile.— The velocity is given, in terms of *Y*, by the following series expansion

$$V_x = 12Y(1 - 2Y) + \sum_{i=1}^{\infty}\frac{2}{\alpha_i^2}\left\{\frac{\cos[\alpha_i(4Y - 1)]}{\cos(\alpha_i)} - 1\right\}\exp\left[-\alpha_i^2 Z\right] \quad [44]$$

in which the eigenvalues are the roots of

$$\tan(\alpha_i) = \alpha_i \quad [45]$$

Introducing the first derivative of equation 44, evaluated at $Y = 0$, into equation 8 and taking into account equation 45 results in

$$\varepsilon = 12 + 8\sum_{i=1}^{\infty}\exp\left[-\alpha_i^2 Z\right] \quad [46]$$

The relationship between X^* and Z is given by

$$X^* = \int_0^Z \frac{\int_{1/4}^{1/2}\left(2V_x - 1.5V_x^2\right)\frac{\partial V_x}{\partial Z}dY}{\partial V_x/\partial Y\big|_{Y=1/2} + \int_{1/4}^{1/2}\left(\partial V_x/\partial Y\right)^2 dY} dZ \quad [47]$$

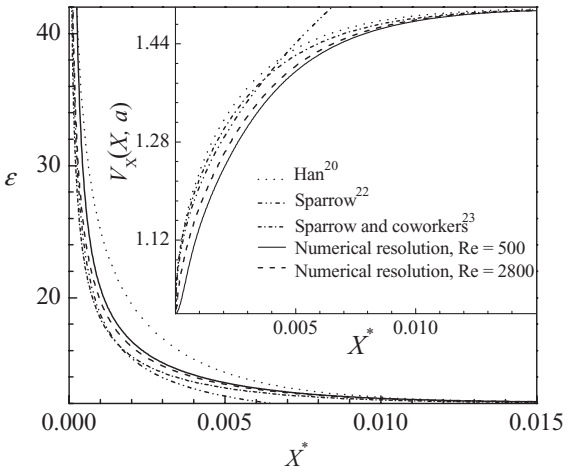

Figure 2. Comparison of the slope in the velocity profile at the electrode surface as a function of the dimensionless axial position for different theoretical models. Inset: dimensionless velocity in the core.

Introducing equation 46 into equation 21 yields

$$Sh_x\, Sc^{-1/3} = \frac{\sqrt{12 + 8\sum_{i=1}^{\infty}\exp\left(-\alpha_i^2 Z\right)}}{\Gamma(4/3)\left[9\int_0^{X^*}\sqrt{12 + 8\sum_{i=1}^{\infty}\exp\left(-\alpha_i^2 Z\right)}dX^*\right]^{1/3}} \quad [48]$$

Figure 2 compares ε according to equations 34, 41 and 46 with the numerical solution of equations 9, 22 and 23, which were simultaneously solved by means of an implicit-explicit finite difference method according to Griebel and coworkers[24] and Strang,[25] using a subroutine written in Matlab for a rectangular region. It was assumed that the velocity profile is uniform along the entrance and at the outlet, large X^*, the gradients of the velocities are zero. The no-slip condition was imposed on the electrode surface, and the initial condition was $V_x = V_y = 0$ in the entire domain. The discretization was $dX = 1.875 \times 10^{-5}$ Re, $dY = 5 \times 10^{-3}$ and $dT = 2.5 \times 10^{-6}$ Re. The calculation was performed until the difference between the recent values with the previous ones was lower than 1×10^{-6}. The inset in Figure 2 shows the velocity in the core. It can be observed that the predictions of the Sparrow and coworkers[23] are close to the numerical procedure and the agreement between both is better when the Reynolds number is increased. Likewise, the differences between the analytical models with the numerical one decrease at high X^* values. However, ε according to the numerical model is between the predictions of Sparrow and coworkers[23] and Han.[20] Then, it can be expected that the mass transfer behavior at the electrode surface under developing flow conditions must be comprised between those given by equations 38 and 48.

Figure 3 reports the local mass transfer behavior according to equations 26, 31, 38, 43 and 48, where the last two equations are very close. It can be observed that the proposals according to the velocity profiles of Han[20] and Sparrow and coworkers[23] show a similar performance in all points along the reactor. It must be emphasized, in accordance with Figure 2, that the numerical solution of the hydrodynamic equations shows a behavior between equations 38 and 48. Likewise, equations 26, 38 and 48 agree at high values of X^*, when the hydrodynamics becomes developed. The inset in Figure 3 explodes the abscissa range, where at X^* values higher than 1×10^{-3} equations 38 and 48 can be approached by equation 26, valid for developed flow, with an error lower than 10%. However, under developing laminar flow conditions the predictions according to equations 31, 38 and 48 are very close. Then, it must be inferred that the exponent of the Reynolds number in empirical laminar mass transfer correlations must ranged from 1/2, equation 31 according to the boundary layer theory, to 1/3,

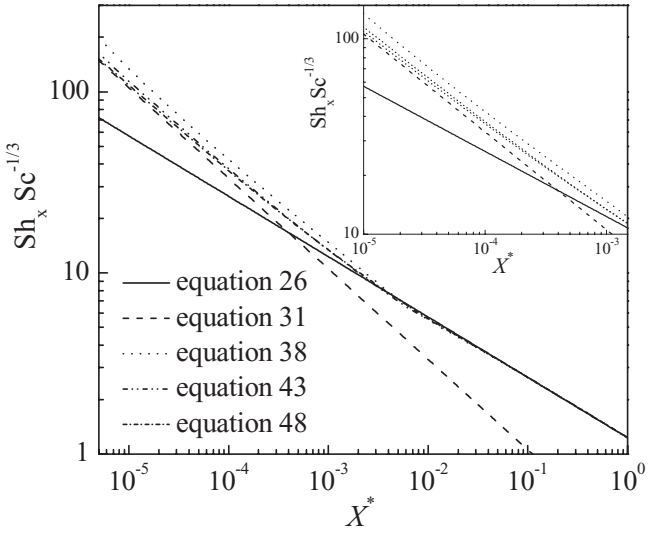

Figure 3. Comparison of the local mass transfer behavior according to different analytical models.

equation 26 under developed flow conditions. Higher values of the exponent in the Reynolds number must be attributed to the effect of the flow distributor on the mass transfer at the reactor inlet and cannot be assigned to the development of the hydrodynamics inside the equipment.

Experimental

All experiments were performed in an electrochemical reactor with parallel plate electrodes, as shown in Figure 4. The reactor was made of acrylic material with both electrodes of nickel, 100 mm width and 250 mm long, arranged in a filter press configuration. The anode, a sheet of 1 mm thick, was electrically fed along its two lateral sides by means of copper current feeders, which were connected to the dc power supply at both ends to ensure isopotentiality of the metal phase. The cathode was made of 25 nickel segments, 100 mm width, 9.5 mm high and 1 mm thick, which were insulated from one another by an epoxy resin of about 0.5 mm thick. The surface of the working electrode was polished to a bright mirror finish with slurry of 0.3 μm alumina powder and it was washed with distilled water. Calibrated resistors, 0.58 Ω resistance, were inserted between the back side of each segment and the cathodic current feeder, which was electrically connected at both ends. By measuring the ohmic drop in the resistors, it was possible to determine the axial current distribution and to calculate the local mass transfer coefficient according to:

$$k_{m,x} = \frac{I_{lim}}{\nu_e F S c} \qquad [49]$$

The effect of the calibrated resistors on the current distribution can be neglected due to the small value of their ohmic drop, approximately 10 mV, in comparison with that in the electrolyte. The data acquisition was performed using a computer controlled, home made analog multiplexer. The experiments were carried out potentiostatically at −0.3 V, the cathodic potential was controlled against a saturated calomel electrode connected to a Haber-Luggin capillary positioned in the middle region of the cathode. However, the cathodic potential was also measured near to the reactor entrance and at the reactor exit in order to insure that all the segments in the cathode were under limiting current conditions. The lower and upper parts of the reactor present chambers, of triangular cross-sectional area, with perpendicular nozzles for the inlet and outlet of the electrolyte, which is represented in the exploded view of Figure 4c. The counter electrode in the inlet and outlet chambers was coated with a silicone-based resin in order to make it

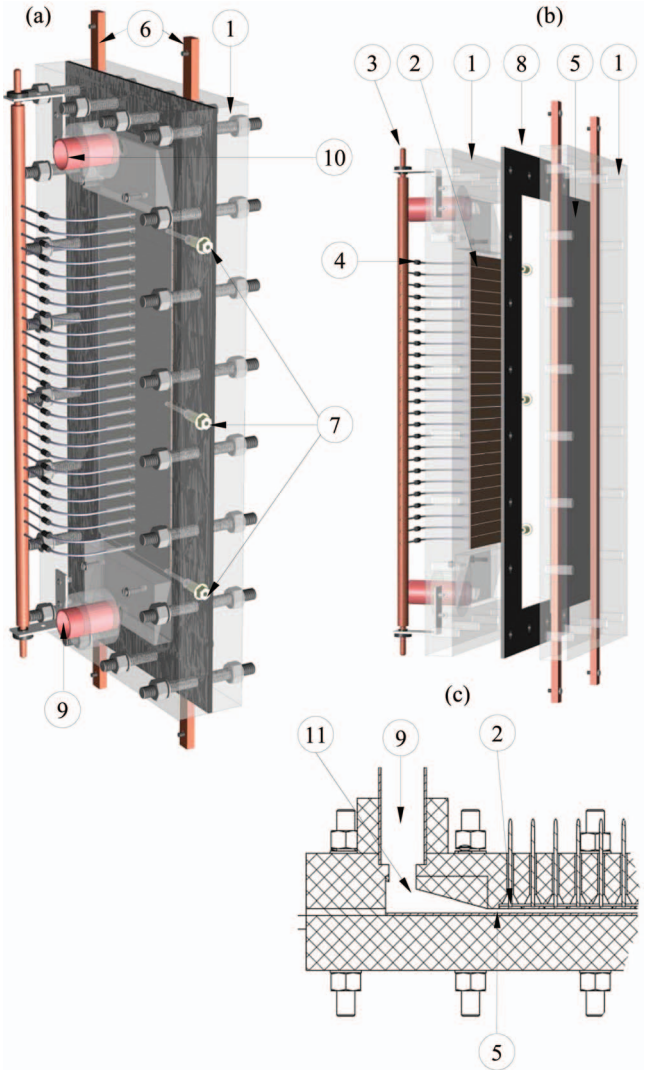

Figure 4. (a) Schematic representation of the parallel plate electrochemical reactor. (b) Exploded view of the reactor. (c) Cross-section showing the electrolyte inlet chamber in the reactor. 1, plates; 2, segmented electrodes; 3, current feeder to the working electrode; 4, calibrated resistors; 5, counter electrode; 6, electrical connection to the counter electrode; 7, Luggin capillaries; 8, gasket; 9, electrolyte inlet; 10, electrolyte outlet; 11, electrolyte inlet chamber.

non-conductive. The interelectrode gap was fixed by the thickness of the gasket.

The reactor was made part of a flow circuit system, sketched in Figure 5, consisting of a pump, a flowmeter, a reservoir and connections to maintain the temperature at the preset value, 30°C. The test reaction was the electrochemical reduction of ferricyanide from solutions with $[K_3Fe(CN)_6] \cong 0.01$ mol dm^{-3}, $[K_4Fe(CN)_6] \cong 0.01$ mol dm^{-3}, in 0.65 mol dm^{-3} of K_2CO_3 as supporting electrolyte, while the reverse reaction occurred at the anode. However, some experiments were performed using the conventional supporting electrolyte of NaOH. Table I summarizes the composition and physicochemical properties of the solutions, which were measured in the laboratory. Samples of the solution were taken from the reservoir after each experiment and the ferricyanide concentration was spectrophotometrically determined using a Perkin-Elmer model Lambda 20 double-beam UV-Vis Spectrophotometer with 10 mm glass absorption cells and the supporting electrolyte was used as blank. The measurements were performed at a wavelength of 422 nm, where it is possible to determine the ferricyanide concentration without any interference of ferrocyanide. Nitrogen was bubbled in the reservoir for 1 h prior to

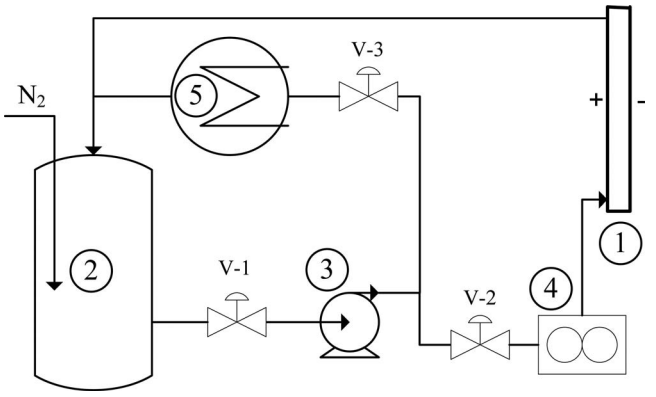

Figure 5. Scheme of the electrolyte circulation system. 1, electrochemical reactor; 2, reservoir; 3, pump; 4, flowmeter; 5, thermostat. V-1, V-2, V-3, valves.

the experiment in order to remove the dissolved oxygen. The same behavior was observed when the experiments were performed with the reactor in horizontal or vertical position and also with upwards and downwards flow.

Results and Discussion

Experiments with a rotating disk electrode.— Prior to the mass transfer studies at parallel plate electrodes, the electrochemical behavior of the test reaction was studied at rotating disk electrodes, 3 mm diameter, of nickel, gold and platinum. Figure 6 shows a set of polarization curves using $[K_3Fe(CN)_6] \cong 0.01$ mol dm^{-3}, $[K_4Fe(CN)_6] \cong 0.01$ mol dm^{-3}, in 0.65 mol dm^{-3} of K_2CO_3 as supporting electrolyte. In all cases a well defined limiting current density can be observed. The curves coincide for platinum and gold, and for nickel at potentials more negative than −0.1 V a limiting current density is achieved, which is very close to that of the other materials. The current as a function of time for the reduction of ferricyanide at nickel and platinum rotating disk electrodes is given in the inset of Figure 6, where it is observed that both materials show a similar and constant current density during a long time. Thus, taking into account the economic aspect, nickel can be chosen as an appropriate material to make the segments of the parallel plate electrode reactor when ferricyanide reduction with K_2CO_3 as supporting electrolyte is used as test reaction for mass transfer studies.

Mass transfer studies with the segmented parallel plate reactor.— Figure 7 shows a typical curve of the ratio between the local Sherwood number and its mean value as a function of the axial position in the reactor. The predictions according to equations 26, 31, 38 and 48 are also reported; where it can be seen that the mass transfer distribution according to equations 38 and 48, valid for developing flow, is less uniform than that given for fully developed flow, equation 26. Likewise, for $x/L > 0.15$ the mass transfer distribution given by equations 38 and 48 is lower than that for fully developed flow,

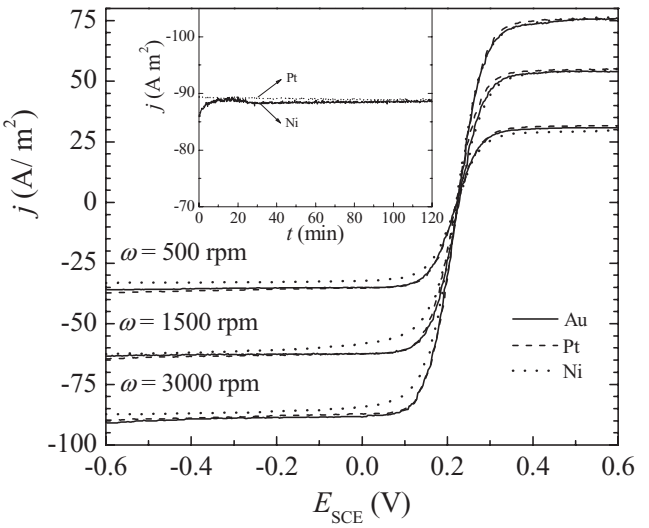

Figure 6. Polarization curves for the ferricyanide-ferrocyanide redox system at a rotating disk electrode of different electrode materials. $[K_3Fe(CN)_6] \cong 0.01$ mol dm^{-3}, $[K_4Fe(CN)_6] \cong 0.01$ mol dm^{-3}, in 0.65 mol dm^{-3} of K_2CO_3 as supporting electrolyte. Temperature = 30 °C. Potential sweep rate: 5 mV s^{-1}. Inset: Current as a function of time, ω = 3000 rpm, $E_{SCE} = -0.3$ V.

because the average mass transfer coefficient is higher at developing flow conditions. The experimental points are properly represented by equations 38 and 48.

Figure 8 compares the local mass transfer results with the behavior according to different theoretical models. The last rows in Table I summarize the experimental conditions reported in Figure 8. The hydrodynamic entrance length reported in Table I, according to Sparrow and coworkers,[23] verifies that in some experiments a significant part of the reactor is under developing flow conditions. The hydraulic diameter was varied by changing the thickness of the gasket between both plate electrodes. It can be observed that the models using the velocity profiles proposed by Han[20] and Sparrow and coworkers[23] show a close agreement with the experimental results. Moreover, the prediction according to equation 26 only is appropriate at high values of X^*. Likewise, the inset in Figure 8 shows the residues for equations 48 demonstrating that the model predictions are appropriate from the statistical point of view.

The global mass transfer results are compared with theoretical ones in Figure 9, where a similar situation to Figure 8 is observed, that is a close agreement between the experimental points with the mass transfer coefficients based on the velocity profiles of Han[20] and Sparrow and coworkers.[23] Likewise, for abscissa values higher than 0.05 the global mass transfer coefficients based on equations 38 and 48 can be approached by equation 27.

Comparison between theoretical models and previous experimental results.— Figure 10 compares experimental results reported by Qi

Table I. Properties of the electrolytes and summary of experimental conditions.

	Electrolyte 1	Electrolyte 2
Composition	$[K_3Fe(CN)_6] = 0.01$ M $[K_4Fe(CN)_6] = 0.01$ M $[K_2CO_3] = 0.65$ M	$[K_3Fe(CN)_6] = 0.1$ M $[K_4Fe(CN)_6] = 0.1$ M $[NaOH] = 0.5$ M
Kinematic viscosity (m^2/s)	1.31×10^{-6}	8.80×10^{-7}
Diffusion coefficient (m^2/s)	8.10×10^{-10}	7.50×10^{-10}
Sc	1617	1173
Re range ($d_h = 3.54$ mm), [L_d range] (mm)	282-1434, [11-55]	372-2231, [14-85]
Re range ($d_h = 7.32$ mm), [L_d range] (mm)	276-1406, [22-110]	
Re range ($d_h = 10.96$ mm), [L_d range] (mm)	271-962, [32-112]	

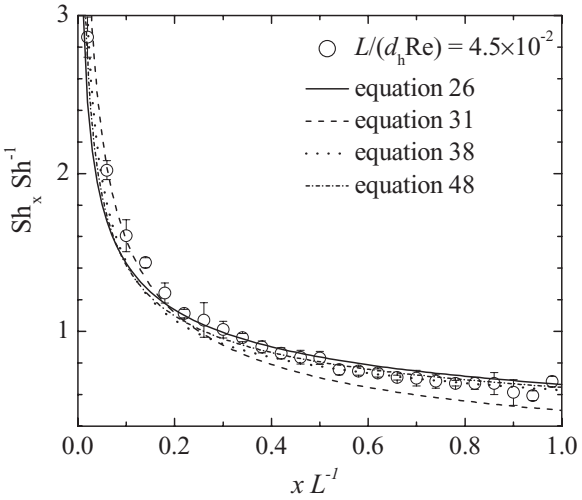

Figure 7. Ratio between the local Sherwood number to the global Sherwood number as a function of the axial position in the reactor for a typical experiment and comparison with theoretical models.

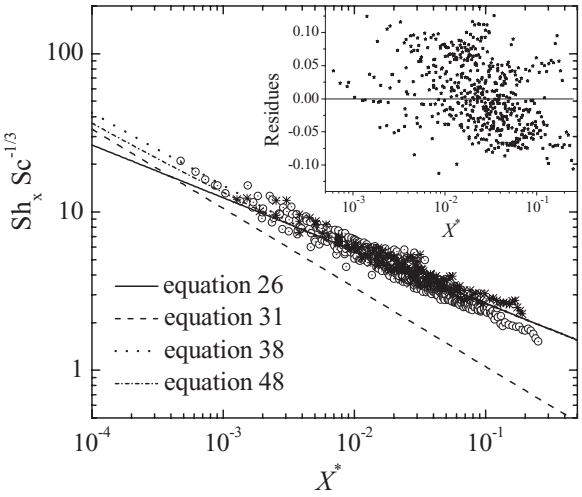

Figure 8. Comparison of the local mass transfer results with theoretical models. ⊙, K_2CO_3 0.65 M as supporting electrolyte; ✳, NaOH 0.5 M as supporting electrolyte.

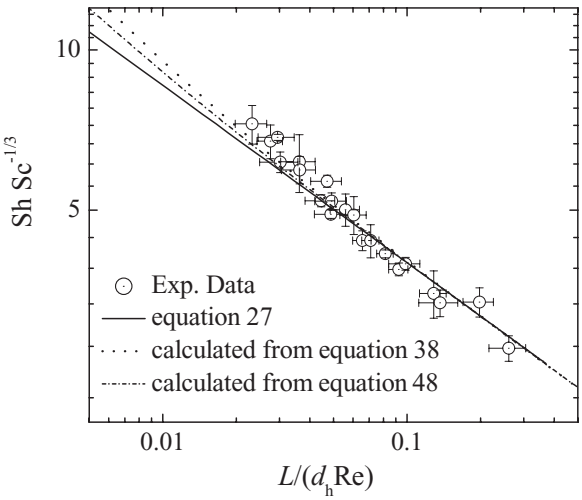

Figure 9. Comparison of the global mass transfer results with theoretical models.

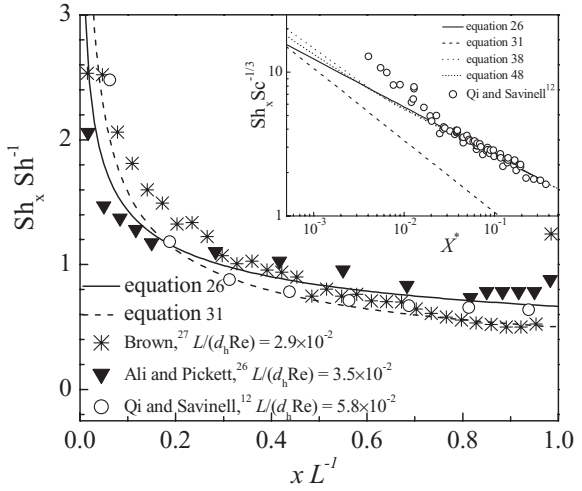

Figure 10. Comparison of results from the literature with the theoretical models.

and Savinell,[12] Ali and Pickett[26] and Brown,[27] for similar $L/(d_h\,\mathrm{Re})$ values, with the theoretical predictions according to equations 26 and 31. The inset of Figure 10 corresponds to the data of Qi and Savinell.[12] In all cases the most important deviations of the experimental results with respect to the theoretical values are observed at the entrance or exit regions, which can be attributed to the effect of the flow distributors on the mass transfer performance. Likewise, for copper deposition on a horizontal cathode in the laminar range of flow, Wranglén and Nilsson[28] reported that the limiting current density increases linearly with $\mathrm{Re}^{1/2}$ and with a slightly greater slope than that calculated for a plane plate without side walls. Comparing these results with those of the present paper it is concluded that special attention must be paid to the design of the flow distributors in order to obtain predictable mass transfer coefficients under developing flow conditions.[29]

Conclusions

(a) Under developing laminar flow conditions the mass transfer coefficients can be predicted using analytical expressions for the velocity profiles when the flow distributors are properly designed, that is a uniform flow along the electrode width is provided.

(b) The exponent in the Reynolds number ranges from 1/3 to 1/2 for developing laminar flow conditions. Higher values indicate an effect of the flow distributors on the reactor hydrodynamics.

(c) When the experimental data of mass transfer as a function of the axial position are represented in a double logarithmic plot, the slope at low X^* is 1/2 and it approaches 1/3 at higher values. Then, the linearization of the experimental data gives a slope between these two limiting values.

(d) Under developing laminar flow, the calculation of the local mass transfer coefficient with the conventional equation 26 yields an error lower than 10% for X^* higher than 1×10^{-3}. Likewise, the global mass transfer coefficient can be approximated by equation 27 when $L/(d_h\,\mathrm{Re})$ is higher than 5×10^{-2}.

(e) The use of the implicit analytical equations, equations 38, 43 and 48, is a fast, accurate and simple way for design, optimization and process control of a parallel plate electrochemical reactor under mass transfer control, with a developing flow region as is usual in industrial practice.

List of Symbols

a	one half of the interelectrode gap, m
c	concentration, $\mathrm{mol/m^3}$
C	dimensionless concentration $= c/c(0)$
C_s	dimensionless concentration at the electrode surface
d_h	hydraulic diameter $= 4a$, m

D	diffusion coefficient, m^2/s
E_{SCE}	cathode potential referred to Saturated Calomel Electrode, V
F	Faraday constant, 96485 C/mol
I_{lim}	limiting current at each segment, A
j	current density, A/m^2
k_m	mass transfer coefficient (m s^{-1})
L	electrode length, m
L_d	hydrodynamic entrance length, mm
p	pressure, Pa
P	dimensionless pressure $= p/\rho {v_{av}}^2$
Re	Reynolds number $= v_{av} d_h/\nu$
S	surface area of each segment, m^2
Sc	Schmidt number $= \nu/D$
Sh	Sherwood number $= k_m d_h/D$
t	time, s or min
T	dimensionless time $= t v_{av}/d_h$
v	flow velocity, m/s
V	dimensionless velocity $= v/v_{av}$
x	axial coordinate, m
X	dimensionless axial coordinate $= x/d_h$
X^*	dimensionless variable $= X/\mathrm{Re}$
y	axial coordinate, m
Y	dimensionless axial coordinate $= y/d_h$
Z	variable employed in the integration of equation 47

Greek Characters

α_i	eigenvalues given by equation 45
β	dimensionless function given by equation 35
γ	dimensionless function given by equation 36
Γ	gamma function
δ_h	thickness of the hydrodynamic boundary layer, m
ε	dimensionless function defined by equation 8
ν	kinematic viscosity, m^2/s
ν_e	charge number of the electrode reaction
ξ	dimensionless variable defined by equation 13
ϕ	dimensionless function given by equation 37
ω	rotation speed, rpm

Subscripts

av	average value
max	maximum value
x	the variable is referred to the x coordinate
y	the variable is referred to the y coordinate

Acknowledgments

This work was supported by the Agencia Nacional de Promoción Científica y Tecnológica (ANPCyT), Consejo Nacional de Investigaciones Científicas y Técnicas (CONICET) and Universidad Nacional del Litoral (UNL) of Argentina.

References

1. M. J. Mader, C. W. Walton, and R. E. White, *J. Electrochem. Soc.*, **133**, 1124 (1986).
2. S. Rayman and R. E. White, *J. Electrochem. Soc.*, **156**, E96 (2009).
3. D. J. Pickett, *Electrochemical Reactor Design*, 2nd ed., Elsevier, Amsterdam (1979), chapter 4.
4. S. Moldoveanu, G. S. Handler, and J. L. Anderson, *J. Electroanal. Chem.*, **179**, 119 (1984).
5. V. Edwards and J. Newman, *J. Electrochem. Soc.*, **134**, 1181 (1987).
6. M. Georgiadou, *J. Electrochem. Soc.*, **144**, 2732 (1997).
7. M. Georgiadou, *Electrochim. Acta*, **48**, 4089 (2003).
8. I. Roušar, J. Hostomský, V. Cezner, and B. Števerák, *J. Electrochem. Soc.*, **118**, 881 (1971).
9. D. J. Pickett and B. R. Stanmore, *J. Appl. Electrochem.*, **2**, 151 (1972).
10. S. Mohanta and T. Z. Fahidy, *Electrochim. Acta*, **21**, 143 (1976).
11. D. J. Pickett and K. L. Ong, *Electrochim. Acta*, **19**, 875 (1974).
12. J. Qi and R. F. Savinell, *J. Appl. Electrochem.*, **20**, 885 (1990).
13. L. Vázquez, A. Alvarez-Gallegos, F. Z. Sierra, C. Ponce de León, and F. C. Walsh, *Electrochim. Acta.*, **55**, 3437 (2010).
14. L. Vázquez, A. Alvarez-Gallegos, F. Z. Sierra, C. Ponce de León, and F. C. Walsh, *Electrochim. Acta.*, **55**, 3446 (2010).
15. A. Acrivos, *Phys. Fluids*, **3**, 657 (1960).
16. F. M. White, *Viscous Fluid Flow*, 3rd ed., Mc Graw Hill, Boston (2005), p. 112.
17. R. B. Bird, W. E. Stewart, and E. N. Lightfoot, *Transport Phenomena*, 2nd ed., John Wiley & Sons, New York (2002), p. 137.
18. E. R. Eckert and R. M. Drake, *Heat and mass transfer*, 2nd ed., McGraw-Hill, New York (1959), p. 176.
19. G. V. Levich, *Physicochemical Hydrodynamics*, Prentice-Hall, Englewood Cliffs (1962), p. 87.
20. L. S. Han, *J. Appl. Mech.*, **27**, 403 (1960).
21. L. A. Glasgow, *Transport Phenomena: an introduction to advanced topics*, John Wiley & Sons, New York (2010), p. 36.
22. E. M. Sparrow, *Analysis of Laminar Forced-convection Heat Transfer in Entrance Region of Flat Rectangular Ducts, NACA Technical Note* 3331, Washington, D.C. (1955).
23. E. M. Sparrow, S. H. Lin, and T. S. Lundgren, *Phys. Fluids*, **7**, 338 (1964).
24. M. Griebel, T. Dornseifer, and T. Neunhoeffer, *Numerical Simulation in Fluid Dynamics: A Practical Introduction*, SIAM, Philadelphia (1998), p. 32.
25. G. Strang, *Computational Science and Engineering*, Wellesley-Cambridge press, Wellesley (2007), p. 533.
26. M. S. Ali and D. J. Pickett, *Chem. Eng. Res. Bull. (Dacca)*, **7**, 1 (1985).
27. C. J. Brown, D. Pletcher, F. C. Walsh, J. K. Hammond, and D. Robinson, *J. Appl. Electrochem.*, **22**, 613 (1992).
28. G. Wranglén and O. Nilsson, *Electrochim. Acta.*, **7**, 121 (1962).
29. Á. Frías-Ferrer, J. González-García, V. Sáez, C. Ponce de León, and F. C. Walsh, *AlChE J.*, **54**, 811 (2008).